Στις 12:20 μ.μ. Τετάρτη, 1 Ιουνίου 2016, ο/η Composite Structures <ees.cost.0.39acd0.0c89750d@eesmail.elsevier.com> έγραψε:

Ms. Ref. No.: COST-D-16-00674
Title: Effect of waviness and orientation of carbon nanotubes on random apparent material properties and RVE size of CNT reinforced composites
Composite Structures

Dear Dr. Dimitrios Savvas,

I am pleased to inform you that your paper "Effect of waviness and orientation of carbon nanotubes on random apparent material properties and RVE size of CNT reinforced composites" has been accepted for publication in Composite Structures.

Your accepted manuscript will now be transferred to our production department and work will begin on creation of the proof. If we need any additional information to create the proof, we will let you know. If not, you will be contacted again in the next few days with a request to approve the proof and to complete a number of online forms that are required for publication.

Below are comments from the editor and reviewers.

When your paper is published on ScienceDirect, you want to make sure it gets the attention it deserves. To help you get your message across, Elsevier has developed a new, free service called AudioSlides: brief, webcast-style presentations that are shown (publicly available) next to your published article. This format gives you the opportunity to explain your research in your own words and attract interest. You will receive an invitation email to create an AudioSlides presentation shortly. For more information and examples, please visit http://www.elsevier.com/audioslides.

Thank you for submitting your work to Composite Structures.

Yours sincerely,

Antonio J. M. Ferreira
Editor
Composite Structures

Comments from the editor:

Interesting paper, accepted in the present form

Effect of waviness and orientation of carbon nanotubes on random apparent material properties and RVE size of CNT reinforced composites

Dimitrios Savvas[a,*], George Stefanou[b], Vissarion Papadopoulos[a], Manolis Papadrakakis[a]

[a]*Institute of Structural Analysis & Antiseismic Research, National Technical University of Athens, 9 Iroon Polytechneiou, Zografou Campus, 15780 Athens, Greece*
[b]*Institute of Structural Analysis & Dynamics of Structures, Department of Civil Engineering, Aristotle University of Thessaloniki, 54124 Thessaloniki, Greece*

Abstract

In this work, the Hill-Mandel macro-homogeneity condition is used to link the micromechanical characteristics of carbon nanotube reinforced composites (CNT-RCs) with the random variation of their material properties at the macroscale. To this purpose, a computational procedure is proposed for the determination of mesoscale random fields describing the spatial variation of the components of the apparent elasticity tensor from a variable number of statistical volume elements (SVEs). Mesoscale images of composites are examined with specific weight fraction (%wt) of randomly scattered CNTs. The cases of randomly oriented and unidirectionally aligned CNTs with random wavy and straight geometry are considered. A stochastic description of the random CNT waviness is adopted based on real measurements. The proposed approach takes into account the local weight fraction variability by processing microstructural models extracted directly from the mesoscale composite images, using a standard moving window technique. Computational homogenization is then applied on a series of SVE finite element models using both kinematic and static uniform boundary conditions. The response statistics of the SVE models are obtained with Monte Carlo simulation (MCS). In this way, the statistical characteristics of the upper and lower bounds of the apparent material properties are effectively computed. The representative

*Corresponding author
Email address: dimitriosavvas@yahoo.gr (Dimitrios Savvas)

volume element (RVE) size is defined within a prescribed tolerance, by examining the convergence of these two bounds with respect to the mesoscale size. The effect of waviness and orientation of CNTs on the mechanical responses, mesoscale random fields and RVE size of the CNT-RC is particularly highlighted.

Keywords: Carbon nanotubes, Random Composites, Apparent Properties, Mesoscale random fields, RVE size, Monte Carlo Simulation

1. Introduction

In the context of nanocomposite science, carbon nanotubes (CNTs) have gained considerable interest due to their superior mechanical and physical properties. Experimental measurements [1, 2, 3, 4] verified by numerical simulations [5, 6, 7, 8, 9] have determined the stiffness of carbon nanotubes at about 1 TPa and their tensile strength at about 150 GPa. Additionally, their high aspect ratio and low density lead to a low percolation threshold and thus to enhanced thermal and electrical properties in polymer composites [10]. These exceptional characteristics make CNTs ideal reinforcing elements for nanocomposites. The multiscale nature of CNT-reinforced composite (CNT-RC) requires understanding of the material behavior across multiple length scales, from atomistic to macroscopic level in order to determine overall effective properties. Through these scales, various uncertain parameters such as random material and geometric properties of CNTs as well as random distribution, agglomeration and alignment of CNTs are affecting the behavior of the CNT-RCs and must be taken into account in a stochastic analysis setting.

Different multiscale methods have been proposed in the past for modeling CNT-RC materials accounting for the coupling of multiple length scales involved. Among them, concurrent and sequential approaches are the most widely applied [11, 12]. Concurrent multiscale methodologies try to combine molecular dynamics and continuum methods, bridging the atomistic nanoscale to the continuum macroscale. In these approaches, the solution of the atomistic problem provides the boundary conditions or kinematic constraints that must be imposed to the continuum problem. On the other hand, sequential approaches apply a length scale separation and the problem is solved progressively form the lowest scale passing information to its subsequent scale and upwards. Following the latter approach, Odegard et al.

[13] modeled the CNT, the local polymer near the nanotube, and the CNT-polymer interface as an effective continuum fiber. Other researchers followed similar formulations for the modeling of CNT-RC interface [14, 15, 16]. Tserpes et al. [17] proposed a multiscale finite element based RVE model for CNT-RCs integrating nanomechanics and continuum mechanics. In Savvas and Papadopoulos [18] a nonlinear multiscale computational homogenization was proposed for the characterization of the mechanical and damping properties of CNT-RCs considering slippage at CNT/polymer interface.

The effect of random CNT waviness and orientaton on the mechanical and physical properties of CNT-RCs has not been adequately addressed so far. The work of Bradshaw et al. [19] was among the first where a single infinitely long sinusoidal fiber within an infinite matrix was modeled by 3-d finite elements and the effective modulus of the composite with aligned or randomly oriented CNTs was predicted using a Mori-Tanaka scheme. The Mori-Tanaka model was also used by Shi et al. [20] in order to study the effect of a spiral shape CNT and agglomeration on the strength of the composite material. Relative studies where analytical micromechanics models have been implemented for predicting mechanical properties of CNT-RCs can be found in [21, 22, 23]. Despite their efficiency, analytical models are limited to a single CNT with deterministic shape and orientation. In contrast, advanced numerical homogenization schemes can handle more complicated material configurations [24, 25, 26, 27]. Rafiee [28] proposed a stochastic multiscale modeling of CNT reinforced polymers and predicted the Young's modulus of the composite material by considering uncertainties in CNT curvature, agglomeration, dispersion and length. In Su et al. [29] a computational structural modeling of CNT/Al composites was presented where the size, morphology, orientation, location and volume fraction of CNTs were reproduced similarly to the actual microstructure of the composite material. Also, in Dong et al. [30] the elastic modulus and local stress distribution in metal matrix composites with non-straight shape of CNTs were investigated using finite element method (FEM) and a micromechanics model. Stein and Wardle [31] studied the combined effect of CNT waviness and alignment on the effective stiffness of polymer matrix nanocomposites by implementing a stochastic 3-d morphology simulation and an extended rule of mixtures.

Computational homogenization of heterogeneous materials is based on the notion of a representative volume element (RVE), which according to Hill [32], is a sample that is structurally entirely typical of the whole mixture on average, and contains a sufficient number of inclusions for the apparent

overall moduli to be effectively independent of the surface values of traction and displacement, as long as these values are macroscopically uniform. The typical procedure to determine the RVE size and the corresponding effective material properties consists in setting multiple realizations of the composite microstructure followed by finite element simulation and statistical analysis of the results [33, 34, 35]. However, effective properties are valid only at the RVE level. In the case of volumes smaller than the RVE, the continuum description of the heterogeneous material involves statistical volume elements (SVE) and mesoscale random fields of the apparent constitutive properties. A computational approach for the determination of RVE size in composite sheets with non-periodic distributed thin and straight needle-shaped inclusions was presented in Ostoja-Starzewski and Wang [36]. A similar procedure was implemented by Savvas et al. [37] for composites containing circular inclusions, where the effect of local volume fraction variability on the determination of RVE size was also assessed. A statistical RVE definition based on percolation analysis in CNT polymer composites has been presented in Song et al. [38].

This paper proposes a computational procedure for the computation of mesoscale random fields as well as for the determination of RVE size of CNT reinforced composites. Computer-simulated images of composites containing randomly oriented and unidirectionally aligned CNTs with random wavy and straight geometry are generated. A stochastic description of the random CNT waviness is adopted based on real measurements. The proposed approach takes into account the local weight fraction variability, usually present in this type of composite materials due to the random dispersion of CNTs inside the polymer matrix. This is performed by processing microstructural models extracted directly from the generated composite images, using the moving window technique. A computational homogenization scheme is applied on a series of SVE finite element models subjected to kinematic and static uniform boundary conditions. The response statistics of the SVE models are obtained using Monte Carlo simulation (MCS). In this way, the statistical characteristics of the upper and lower bounds of the apparent material properties are effectively computed. The size of the RVE is then defined within a prescribed tolerance, by examining the convergence of these two bounds with respect to the mesoscale size. The effect of waviness and orientation of CNTs on the mechanical responses, mesoscale random fields and RVE size of the CNT-RC is particularly highlighted.

The remaining of the paper is organized as follows: In section 2, some

details on the modeling of CNT-RC RVEs are presented. Section 3 refers to the computation of the local weight fraction variability. The computational procedure for the determination of the RVE size of CNT-RCs is explained in section 4. Numerical results regarding the effect of waviness and orientation of CNTs on the mechanical responses, mesoscale random fields and RVE size of CNT-RCs are included in section 5. Finally, section 6 points out the major conclusions of the present study.

2. Modeling RVEs of CNT-RCs

2.1. Equivalent continuum modeling of CNT

Carbon nanotubes are allotropes of carbon with a cylindrical nanostructure built from a repeated hexagonal pattern of C-C covalent bonds. A single wall CNT (SWCNT) can be also visualized as a tubular structure constructed by rolling up a graphene sheet along a chiral vector. According to the orientation of this chiral vector, CNTs are grouped into armchair, zigzag and chiral. Multiwall CNTs (MWCNTs) are constructed by co-axially situated SWCNTs with different radii connected to each other by weak van der Waals forces.

In the context of CNT modeling, equivalent continuum approaches are more efficient than other atomistic approaches such as molecular dynamics (MD) and are used to simulate larger scale systems and longer time spans. The core principle of the equivalent continuum modeling (ECM) approaches is the replacement of the C-C bonds with energetically equivalent continuum elements. The molecular structural mechanics (MSM) approach proposed by Li and Chou [39] has been broadly used, where the C-C bonds are replaced by 3-d Bernoulli beams. In this way the atomic lattice of a CNT is simulated by a space frame finite element structure which can be further projected into an equivalent beam element (EBE). The axial, bending and torsional stiffness of this equivalent beam are derived from finite element simulation of specific loading cases depicted in Fig. 1. More details on the multiscale modeling of CNTs can be found in Savvas et al. [5] where the derived EBE is used as the basic building element for the construction of full length CNTs at the microscale.

2.2. Stochastic modeling of CNT waviness

Random CNT waviness is modeled as a non-homogeneous stochastic field using the spectral representation method in conjunction with evolutionary

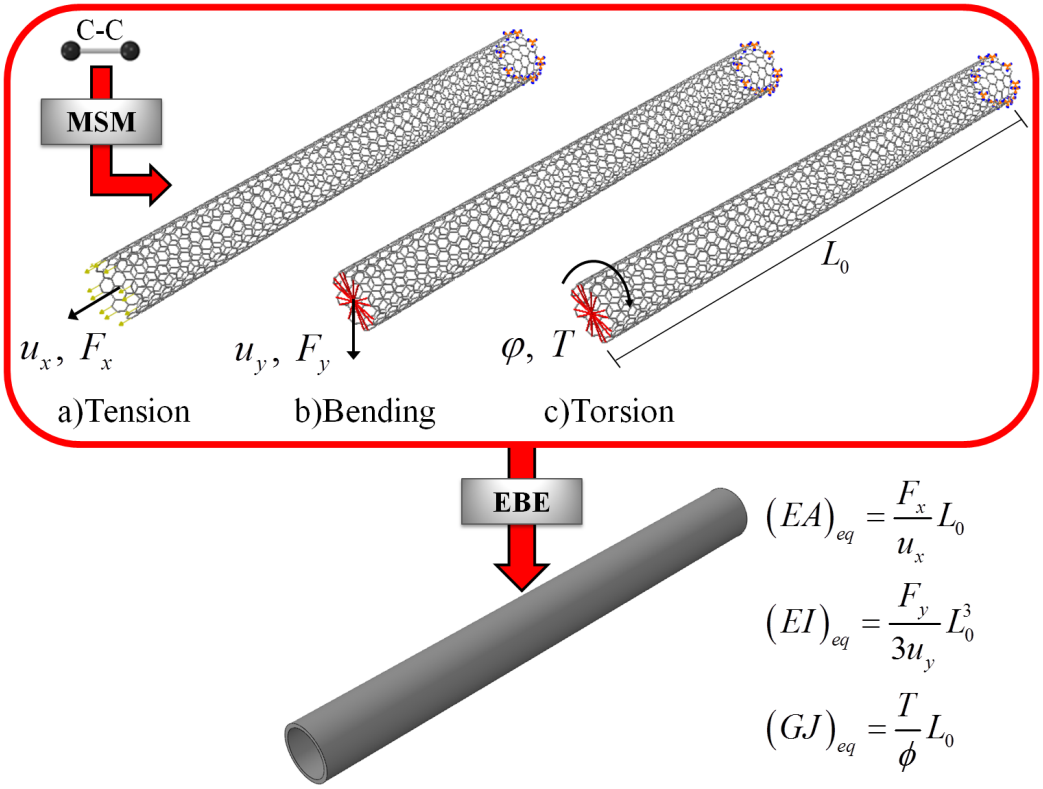

Figure 1: Illustration of the computational procedure for the determination of axial, bending and torsional stiffness of the equivalent beam element.

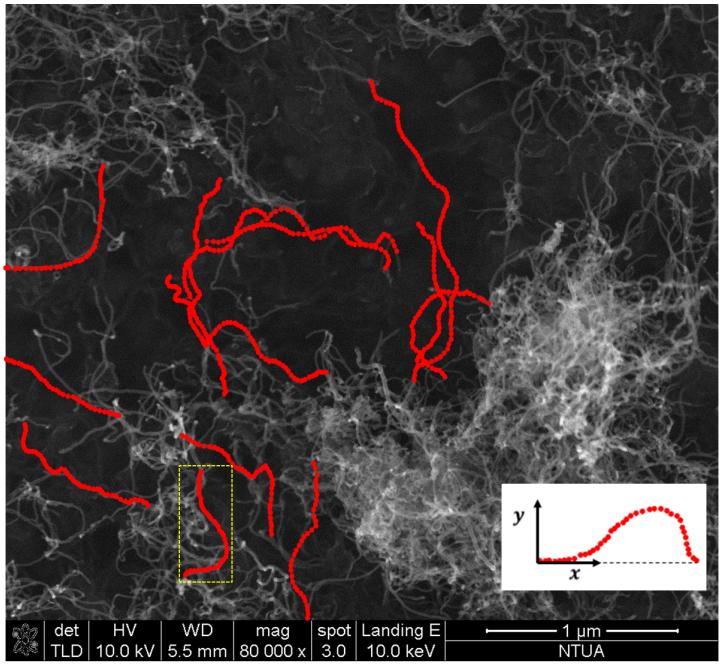

Figure 2: SEM image and processing of wavy geometry of selected CNTs.

power spectra (EPS). The statistical properties of the EPS are derived from processing a number of CNT geometries from scanning electron microscope (SEM) images (Fig. 2).

The EPS depend not only on the frequency ω but also on spatial state variables. In cases of separable or approximately separable EPS, which is the case of geometric imperfections [40] such as the CNT waviness, the corresponding EPS can be expressed as the product of a homogeneous power spectrum $S_h(x)$ and a spatial envelope function $g_h(x)$ as follows:

$$S(\omega, x) = S_h(\omega) \cdot g_h(x) \tag{1}$$

Various methodologies have been proposed in the past for estimating EPS from available experimental measurements, i.e., from real samples of stochastic signals. Among them the most widely used are the short-time Fourier transform and the wavelet-based EPS estimation [41, 42, 43]. The basic disadvantage of these approaches is that they cannot achieve simultaneous resolution in space and frequency domains. A novel methodology was

proposed in Schillinger and Papadopoulos [40] to obtain estimates of EPS of separable processes. This method is based on simple principles of stochastic process theory and for this reason it is easy to implement and computationally efficient, while at the same time proved to be accurate enough with optimum simultaneous resolution in space and frequency [44, 40].

According to this approach an estimate of the first term in Eq. (1) can be readily obtained by averaging the periodograms over the ensemble:

$$\overline{S}_h(\omega) = E\left[\frac{1}{2\pi L}\left|\int_0^L f^{(i)}(x)\cdot e^{-i\omega x}dx\right|\right] \tag{2}$$

where $f^{(i)}(x)$ is a sample of the stochastic field (in particular the wavy geometry of the i^{th} CNT) and $E[\cdot]$ denotes the mathematical expectation. An estimate of the spatial envelope function can be obtained from the distribution of the mean square over the samples as follows:

$$\overline{g}_h(x) = \frac{E\left[|f(x)|^2\right]}{2\int_0^\infty \overline{S}_h(\omega)d\omega} \tag{3}$$

It can be easily shown that an unbiased estimate of the evolutionary power spectra may be obtained as follows:

$$\overline{S}_h(\omega, x) = E\left[\left|f^{(i)}(x)\right|^2\right]\frac{\overline{S}_h(\omega)}{2\int_0^\infty \overline{S}_h(\omega)d\omega} \tag{4}$$

Having estimated the EPS from a number of selected CNTs taken from Fig. 2 samples of wavy CNTs can be generated using Eq. (4) for the spectral representation method, as follows [45]:

$$\hat{f}^{(j)}(x) = \sqrt{2}\sum_{n=0}^{N-1} A_n \cos\left(\omega_n x + \phi_n^{(j)}\right) \tag{5}$$

where

$$\begin{aligned} &A_n = \sqrt{2\overline{S}_h(\omega_n, x)\Delta\omega} && n = 0, 1, ..., N-1 \\ &\omega_n = n\Delta\omega && n = 0, 1, ..., N-1 \\ &\Delta\omega = \frac{\omega_{up}}{N} \\ &A_0 = 0, \quad \overline{S}_h(\omega_0, x) = 0 \end{aligned} \tag{6}$$

The parameter ω_{up} refers to an upper limit of the frequency, beyond which the spectral density function is supposed to be zero. Parameter $\phi_n^{(j)}$ stands for random phase angles in the range $[0,\ 2\pi]$, for the j^{th} sample realization.

2.3. The embedded element technique

To avoid complicated mesh discretization in the FEM analysis of the CNT-RCs the embedded element technique is used where the translational degrees of freedom (dofs) of the embedded element are kinematically constrained to the translational dofs of the host element. Suppose that a CNT is modeled by a 2-d beam element (embedded element) and lies in the composite matrix which is modeled by a quadratic plane elasticity element (host element) as shown in Fig. 3. The dof vector of the embedded element $\boldsymbol{u}_e = [u_a,\ \nu_a,\ u_b,\ \nu_b,\ \theta_a,\ \theta_b]^T$ is kinematically related to an extended dof vector containing both the translational dofs of the host element and the unconstrained rotational dofs of the embedded element $\boldsymbol{u}_h = [u_1,\ \nu_1,\ u_2,\ \nu_2,\ u_3,\ \nu_3,\ u_4,\ \nu_4,\ \theta_a,\ \theta_b]^T$. The kinematic constraint is expressed as follows:

$$\boldsymbol{u}_e = \boldsymbol{N}\boldsymbol{u}_h \tag{7}$$

where

$$\boldsymbol{N}_{6\times 10} = \begin{bmatrix} \boldsymbol{N}_{h\ 2\times 8}^{a} & \varnothing \\ \boldsymbol{N}_{h\ 2\times 8}^{b} & \varnothing \\ \varnothing & \boldsymbol{I}_{2\times 2} \end{bmatrix} \tag{8}$$

and

$$\boldsymbol{N}_h^i = \begin{bmatrix} N_{h1}^i & 0 & N_{h2}^i & 0 & N_{h3}^i & 0 & N_{h4}^i & 0 \\ 0 & N_{h1}^i & 0 & N_{h2}^i & 0 & N_{h3}^i & 0 & N_{h4}^i \end{bmatrix} \tag{9}$$

with $i = a,\ b$ denoting the coordinates $(x_i,\ y_i)$ of the end points of the embedded beam element A and B, respectively where the shape functions of the host element are evaluated. The dof vector of the embedded element is transformed to its local cordinate system using the rotation matrix $\boldsymbol{R}$

$$\boldsymbol{u}_e^{loc} = \boldsymbol{R}\boldsymbol{u}_e \tag{10}$$

with

$$\boldsymbol{R}_{6\times 6} = \begin{bmatrix} \boldsymbol{Q}_{2\times 2} & \varnothing & \varnothing \\ \varnothing & \boldsymbol{Q}_{2\times 2} & \varnothing \\ \varnothing & \varnothing & \boldsymbol{I}_{2\times 2} \end{bmatrix},\quad \boldsymbol{Q} = \begin{bmatrix} \cos\phi & \sin\phi \\ -\sin\phi & \cos\phi \end{bmatrix} \tag{11}$$

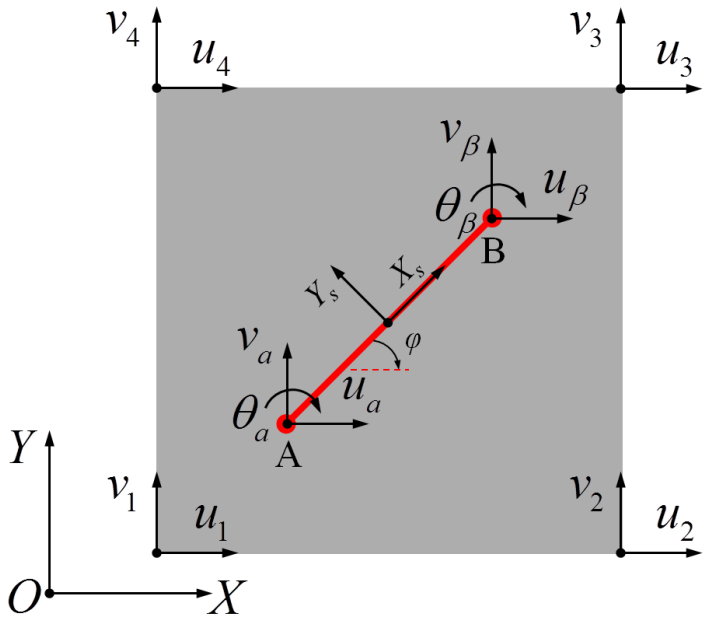

Figure 3: Illustration of the embedded beam element.

The axial strain ε_s at a point $(x_s,\ y_s)$ of the embedded beam element is calculated as:

$$\varepsilon_s = \frac{\mathrm{d}u_s}{\mathrm{d}s} - y_s \frac{\mathrm{d}^2\nu_s}{\mathrm{d}s^2} = \boldsymbol{T}^* \boldsymbol{B}_h^s \boldsymbol{u}_h - y_s \boldsymbol{B}_e^s \boldsymbol{u}_e^{loc} \tag{12}$$

where

$$\boldsymbol{T}^* = \left[\cos^2\phi,\ \sin^2\phi,\ \cos\phi\,\sin\phi\right] \tag{13}$$

and $\boldsymbol{B}_h^s$, $\boldsymbol{B}_e^s$ are matrices containing the spatial derivatives of the shape functions N_h for the host element and N_e for the embedded element, respectively. The overall stiffness matrix is formulated as follows:

$$\boldsymbol{K} = \boldsymbol{K}_h + \boldsymbol{K}_e \tag{14}$$

where

$$\boldsymbol{K}_h = \int_{V_h} \boldsymbol{B}_h^T \boldsymbol{D} \boldsymbol{B}_h dV_h \tag{15}$$

is the stiffness matrix of the host element and

$$\boldsymbol{K}_e = \int_s [\boldsymbol{T}^* \boldsymbol{B}_h^s]^T (EA) [\boldsymbol{T}^* \boldsymbol{B}_h^s] ds + [\boldsymbol{RN}]^T \left[\int_s [\boldsymbol{B}_e^s]^T (EI) [\boldsymbol{B}_e^s] ds \right] [\boldsymbol{RN}] \tag{16}$$

is the stiffness matrix of the embedded element. $\boldsymbol{D}$ is the 2-d elasticity tensor representing the material of the composite matrix, while EA and EI are the axial and bending stiffness of the CNT derived according to the equivalent continuum modeling of section 2.1.

3. Computation of local weight fraction variation

In this section the variability of local weight fraction (wt) of CNTs due to their random distribution inside a polymer matrix is calculated for various computer-simulated composites. The weight fraction is connected to the volume fraction (vf) through the relation:

$$wt = \frac{\alpha}{\nu f + \alpha - 1} \tag{17}$$

where α is the ratio of the density of CNT ($\rho_{cnt} = 1.8\ gr/cm^3$) over the density of the polymer matrix ($\rho_{mtrx} = 1.4\ gr/cm^3$). An algorithm has been implemented which performs the uniform random distribution of an initial amount of 0.2 wt% CNTs inside a rectangular polymer matrix. Four images have been constructed in this way corresponding to composites with a) wavy and randomly oriented, b) wavy and unidirectionally aligned, c) straight and randomly oriented and d) straight and unidirectionally aligned CNTs, which are shown in Fig. 4. All images have dimensions $L_{image} \times L_{image}$ with $L_{image} = 100\ \mu m$ and contain approximately 6000 randomly scattered CNTs with random length $L_{cnt} \in U\,(1,\ 2\ \mu m)$.

The local weight fraction variation is evaluated by processing window models extracted from the composite image using the moving window technique. In this method an initial window of area $L \times L$ is set at a starting point O of the image and then, by moving it over the image by a vector $\vec{\xi_p} = \xi_{x_p}\vec{e_x} + \xi_{y_p}\vec{e_y}$ a set of windows of the same area is extracted (see Fig. 5). The moving step $\Delta\xi$ is assumed to be the same along both directions. This means that $\xi_{x_p} = i\Delta\xi$ and $\xi_{y_p} = j\Delta\xi$, with i, j the number of steps along the x and y directions, respectively. The total number of windows n_w extracting

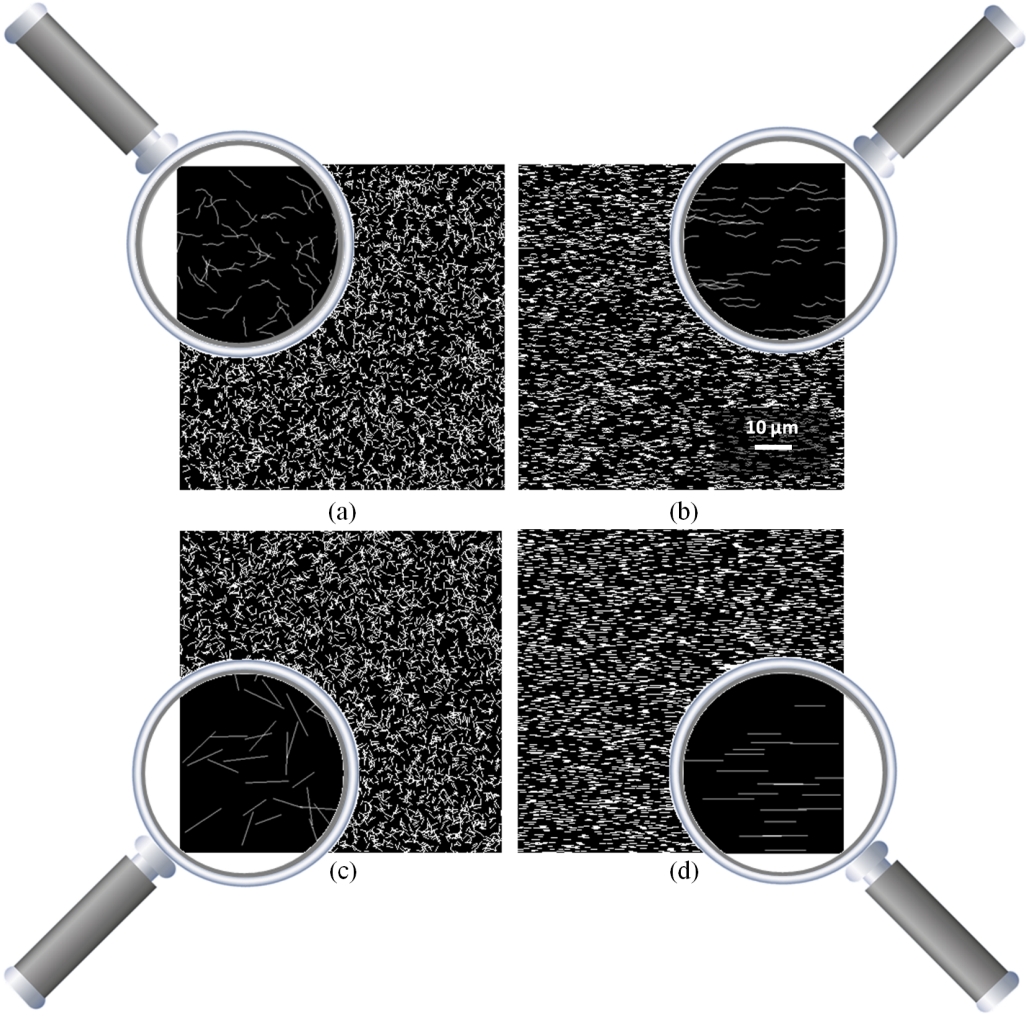

Figure 4: Computer simulated images of random CNT-RCs with 0.2 wt% of a) wavy randomly oriented (image 1), b) wavy unidirectionally aligned (image 2), c) straight randomly oriented (image 3) and d) straight unidirectionally aligned (image 4) CNTs.

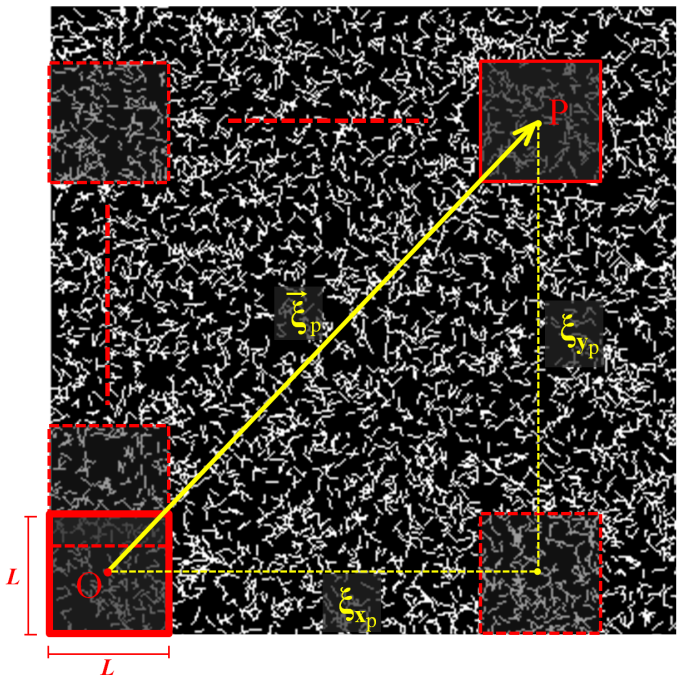

Figure 5: Illustration of the moving window technique.

from the composite image depends on its size L_{image}, the window size L and the selected moving step $\Delta\xi$ as follows:

$$n_w = \left(\frac{L_{image} - L}{\Delta\xi} + 1 \right)^2 \tag{18}$$

By choosing $\Delta\xi = L/4$ with L=2, 5, 10, 25 and 50 μm, 5 sets containing n_w=38809, 5929, 1369, 169 and 25 windows, respectively are extracted. The wt of CNTs is computed in each window by using image analysis tools and Eq. (17). The histograms of the wt with respect to the non-dimensional parameter $\delta = L/d$, where $d = 2$ μm the maximum length of CNTs, are shown in Fig. 6 for each composite image of Fig. 4. As the dispersion of the CNTs within the composite materials is random, it is obvious that there are regions rich or poor in inclusions. This is clearly illustrated in the histograms where a very large variability of wt is observed for the sets containing windows of small size. On the other hand, for large δ the empirical PDFs of wt become very narrow and tend to a spike. These results indicate that wt varies

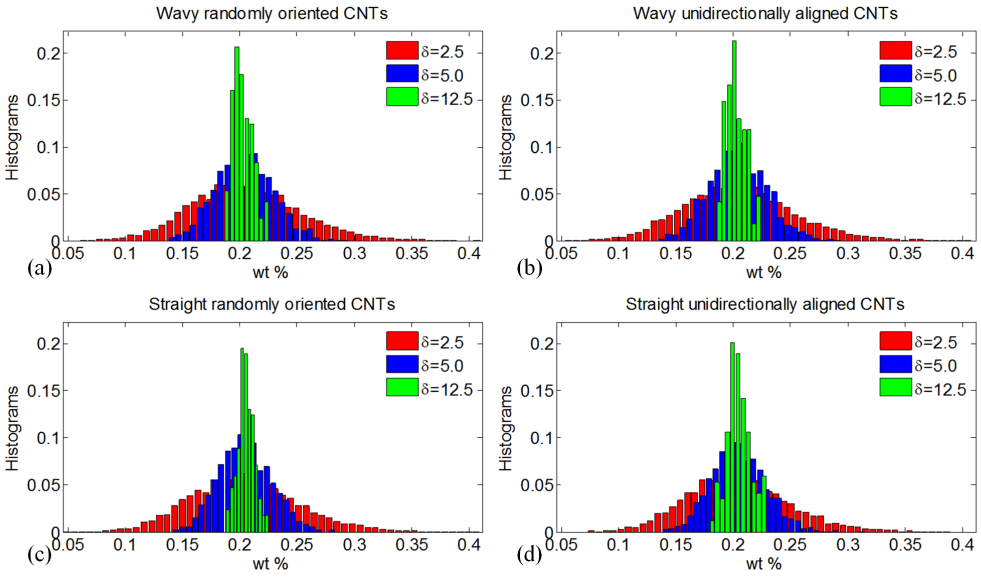

Figure 6: Histograms (relative frequency) of wt for various window sizes δ for a) image 1, b) image 2 c) image 3, d) image 4 of Fig. 4.

significantly with the size and location of the windows. Therefore choosing a relatively small RVE without considering local weight fraction variability can lead to unrealistic estimations of the effective mechanical behavior of composites [46, 47, 37].

4. Computational procedure for RVE determination

4.1. Computation of apparent properties on mesoscale

Miehe and Koch [24] proposed a computational procedure to define apparent properties (homogenized stresses and overall tangent moduli) of microstructures undergoing small strains. They have shown that apparent properties can be defined in terms of discrete forces and stiffness properties on the boundary of discretized microstructures. Using these deformation-driven algorithms, the apparent stiffness or compliance tensor of a mesoscale model of size δ can be calculated by solving a uniform strain or a uniform stress boundary value problem, respectively. These boundary conditions satisfy a priori the Hill-Mandel macro-homogeneity condition [32]. The adopted computational procedure is outlined below for the two cases of uniform boundary

conditions.

4.1.1. Uniform strains

A prescribed uniform strain tensor $\bar{\boldsymbol{\varepsilon}} = [\bar{\varepsilon}_{11} \;\; \bar{\varepsilon}_{22} \;\; 2\bar{\varepsilon}_{12}]^T$ is applied on the boundary ∂B_δ of a discretized mesoscale model through displacement boundary conditions (Dirichlet) in the form:

$$\boldsymbol{u}_b = \boldsymbol{D}_b^T \bar{\boldsymbol{\varepsilon}} \tag{19}$$

where $\boldsymbol{D}_b$ is a geometric matrix which depends on the coordinates of the boundary node b and is defined as:

$$\boldsymbol{D}_b = \frac{1}{2}\begin{bmatrix} 2Y_1 & 0 \\ 0 & 2Y_2 \\ Y_2 & Y_1 \end{bmatrix} \quad \text{with} \quad (Y_1, Y_2) \in \boldsymbol{Y} \tag{20}$$

Note that the stiffness matrix $\boldsymbol{K}$ of the model can be rearranged into submatrices associated with interior nodes i and boundary nodes b. Thus the static problem is denoted by:

$$\begin{bmatrix} \boldsymbol{K}_{ii} & \boldsymbol{K}_{ib} \\ \boldsymbol{K}_{bi} & \boldsymbol{K}_{bb} \end{bmatrix} \begin{bmatrix} \boldsymbol{U}_i \\ \boldsymbol{U}_b \end{bmatrix} = \begin{bmatrix} \boldsymbol{F}_i \\ \boldsymbol{F}_b \end{bmatrix} \tag{21}$$

Then the apparent stiffness tensor $\boldsymbol{C}_\delta^D(\theta)$ of the mesoscale model of size δ under Dirichlet boundary conditions can be calculated in terms of the condensed stiffness matrix $\tilde{\boldsymbol{K}}_{bb} = \boldsymbol{K}_{bb} - \boldsymbol{K}_{bi}\boldsymbol{K}_{ii}^{-1}\boldsymbol{K}_{ib}$ in the form:

$$\boldsymbol{C}_\delta^D(\theta) = \frac{1}{V_\delta}\mathbb{D}\tilde{\boldsymbol{K}}_{bb}\mathbb{D}^T \tag{22}$$

where $\mathbb{D} = [\boldsymbol{D}_1 \; \boldsymbol{D}_2 \; ... \; \boldsymbol{D}_M]$ with M the total number of boundary nodes.

4.1.2. Uniform stresses

A prescribed uniform stress tensor $\bar{\boldsymbol{\sigma}} = [\bar{\sigma}_{11} \;\; \bar{\sigma}_{22} \;\; 2\bar{\sigma}_{12}]^T$ is applied on the boundary surface ∂B_δ of a discretized mesoscale model through traction boundary conditions (Neumann) as follows:

$$\boldsymbol{F}_b = \boldsymbol{S}_b^T \bar{\boldsymbol{\sigma}} \tag{23}$$

where $\boldsymbol{S}_b$ is a matrix depending on the components of the discrete area vector $\mathbf{a}_b$ which is given in terms of the nodal coordinates of the neighboring boundary nodes $b-1$, b and $b+1$ in the form:

$$\mathbf{a}_b = \frac{1}{2}\left[\boldsymbol{Y}_{b+1} - \boldsymbol{Y}_{b-1}\right] \times \boldsymbol{e}_n \tag{24}$$

These nodes are oriented so that the cross product with the Cartesian, out-of-plane, base vector $\boldsymbol{e}_n$ yields $\mathbf{a}_b$ as an outward normal vector at the boundary node b. Thus the matrix $\boldsymbol{S}_b$ is defined as:

$$\boldsymbol{S}_b = \begin{bmatrix} \mathrm{a}_{b_1} & 0 \\ 0 & \mathrm{a}_{b_2} \\ \mathrm{a}_{b_2} & \mathrm{a}_{b_1} \end{bmatrix} \tag{25}$$

Then the apparent compliance tensor $\boldsymbol{S}_\delta^N(\theta)$ of the mesoscale model of size δ under Neumann boundary conditions can be calculated in terms of the condensed stiffness matrix $\tilde{\boldsymbol{K}}_{bb}$ in the form:

$$\boldsymbol{S}_\delta^N(\theta) = \frac{1}{V_\delta}\mathbb{S}\tilde{\boldsymbol{K}}_{bb}^{-1}\mathbb{S}^T \tag{26}$$

where $\mathbb{S} = [\boldsymbol{S}_1\ \boldsymbol{S}_2\ ...\ \boldsymbol{S}_M]$ with M the total number of boundary nodes. For this type of boundary conditions the apparent stiffness tensor is obtained by inverting the compliance tensor of Eq. (26):

$$\boldsymbol{C}_\delta^N(\theta) = \left[\boldsymbol{S}_\delta^N(\theta)\right]^{-1} \tag{27}$$

Dirichlet and Neumann boundary conditions provide upper and lower bounds of the strain energy which converge to each other as the mesoscale size δ is increasing. Thus the following relation holds [48]:

$$\left\{\begin{array}{ll} \frac{1}{2}\left[\bar{\boldsymbol{\varepsilon}} : \boldsymbol{C}_\delta^N(\theta) : \bar{\boldsymbol{\varepsilon}}\right] < \frac{1}{2}\left[\bar{\boldsymbol{\varepsilon}} : \boldsymbol{C}_\delta^D(\theta) : \bar{\boldsymbol{\varepsilon}}\right] & \text{for } \delta \text{ finite} \\ \frac{1}{2}\left[\bar{\boldsymbol{\varepsilon}} : \boldsymbol{C}_\infty^N(\theta) : \bar{\boldsymbol{\varepsilon}}\right] = \frac{1}{2}\left[\bar{\boldsymbol{\varepsilon}} : \boldsymbol{C}_\infty^D(\theta) : \bar{\boldsymbol{\varepsilon}}\right] & \text{for } \delta \to \infty \end{array}\right\} \tag{28}$$

In case of uniaxial strains $\bar{\boldsymbol{\varepsilon}} = \left([1\ \ 0\ \ 0]^T \text{ or } [0\ \ 1\ \ 0]^T\right)$ or simple shear $\bar{\boldsymbol{\varepsilon}} = [0\ \ 0\ \ 1]^T$ the following notation can be used:

$$\boldsymbol{C}_\delta^N(\theta) \leq \boldsymbol{C}_\delta^D(\theta) \tag{29}$$

5. Results and discussion

In this section, the spatial average (mean) of the apparent moduli of the CNT-RC is calculated at each size δ from the n_w corresponding mesoscale models extracted from the moving window technique of section 3. Thus the following formula for the mean can be used:

$$\overline{\boldsymbol{C}_\delta(\theta)} = \frac{1}{n_w}\sum_{p=1}^{n_w} \boldsymbol{C}_\delta\left(\vec{\xi}_p, \theta\right) \tag{30}$$

with $\vec{\xi}_p$ the position vector of the p-th mesoscale window model on the image (see Fig. 5). Following the notation of Eq. (29) the bounds $\overline{\boldsymbol{C}_\delta^N(\theta)}$ and $\overline{\boldsymbol{C}_\delta^D(\theta)}$ are calculated for the axial and shear components of the apparent elasticity tensor. Note that, the computational homogenization of section 4.1 results in an anisotropic apparent elasticity tensor due to the nature of the CNT-reinforcement and spatial randomness. The CNTs chosen for reinforcement are considered multi-walled of type armchair with an outer radius $d_{cnt} \approx 14\ nm$ and Young's modulus $E_{cnt} = 1\ TPa$. The polymer matrix is considered linear elastic with $E_{mtrx} = 1\ GPa$ and Poisson ratio $\nu_{mtrx} = 0.3$. In the following numerical results all the computed components of the apparent elasticity tensor are in GPa.

5.1. Effect of CNT waviness and orientation

The effect of CNT waviness and orientation on the axial (C_{11}) and shear (C_{33}) stiffness component of the apparent elasticity tensor of the composites of section 3, as well as on the determination of the RVE size is illustrated in Fig. 7 and 8, respectively. These figures depict the convergence of the numerical upper (Dirichlet) and lower (Neumann) bounds for $\overline{C_{11}}$ and $\overline{C_{33}}$ with respect to the mesoscale size δ. Figure 7 shows that the composites with unidirectionally aligned CNTs have larger axial stiffness than the composites with randomly oriented CNTs. From the same figure it can be observed that the effect of CNT waviness on the stiffness of the composite is more important in the case of unidirectionally aligned CNTs. On the other hand, Fig. 8 shows that the composites with randomly oriented CNTs have larger shear stiffness than the composites with unidirectionally aligned CNTs. Note that the straight unidirectionally aligned CNTs have no reinforcement effect on the elasticity tensor of the polymer matrix except in the longitudinal direction of the CNTs (axial stiffness component C_{11}). The shear stiffness

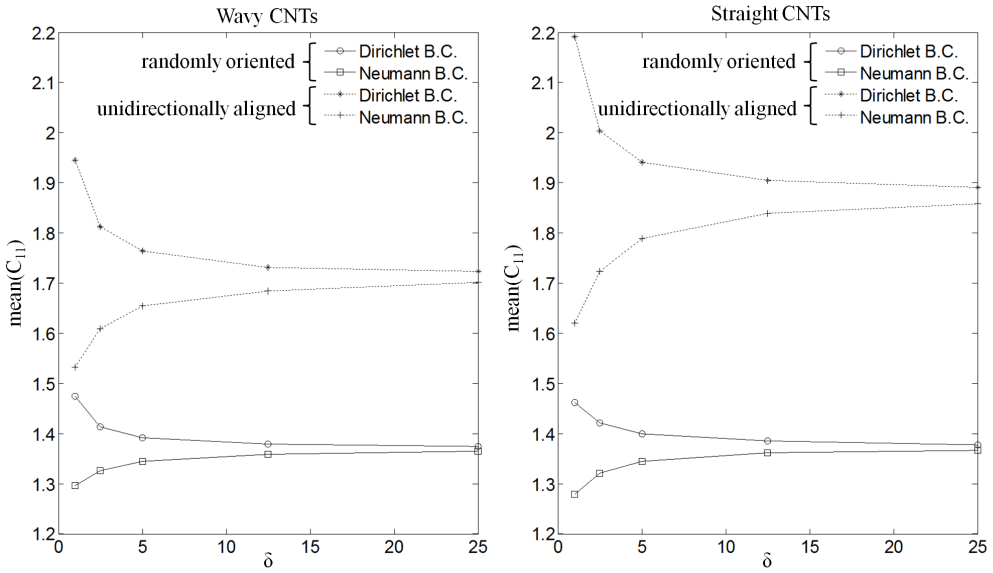

Figure 7: Comparison of numerical bounds of apparent property C_{11} for the composites of a) images 1, 2 and b) images 3, 4.

of the composite with straight unidirectionally aligned CNTs corresponds to that of the polymer matrix which is homogeneous. Therefore C_{33} is in this case an effective property and does not depend on mesoscale size δ.

In Fig. 9 the discrepancy (tolerance) e_δ between the computed numerical bounds of axial and shear stiffness is plotted as a function of δ for each composite (images 1-4 of Fig. 4). The discrepancy is calculated as:

$$e_\delta = \left| \frac{\overline{C_{ij}^D} - \overline{C_{ij}^N}}{\overline{C_{ij}^D}} \right|_\delta \tag{31}$$

where $\overline{C_{ij}^D}$ and $\overline{C_{ij}^N}$ are the components of the spatially averaged apparent elasticity tensor obtained by applying Dirichlet and Neumann boundary conditions, respectively (see section 4.1). Fig. 9 shows that, when the axial stiffness C_{11} is monitored, the case of straight and unidirectionally aligned CNTs leads to relatively slow convergence rate for the RVE size. On the other hand, when the shear stiffness C_{33} is monitored, the case of straight and randomly oriented CNTs leads to relatively slow convergence rate. For example, in order to attain the RVE within a tolerance of 5% when C_{11}

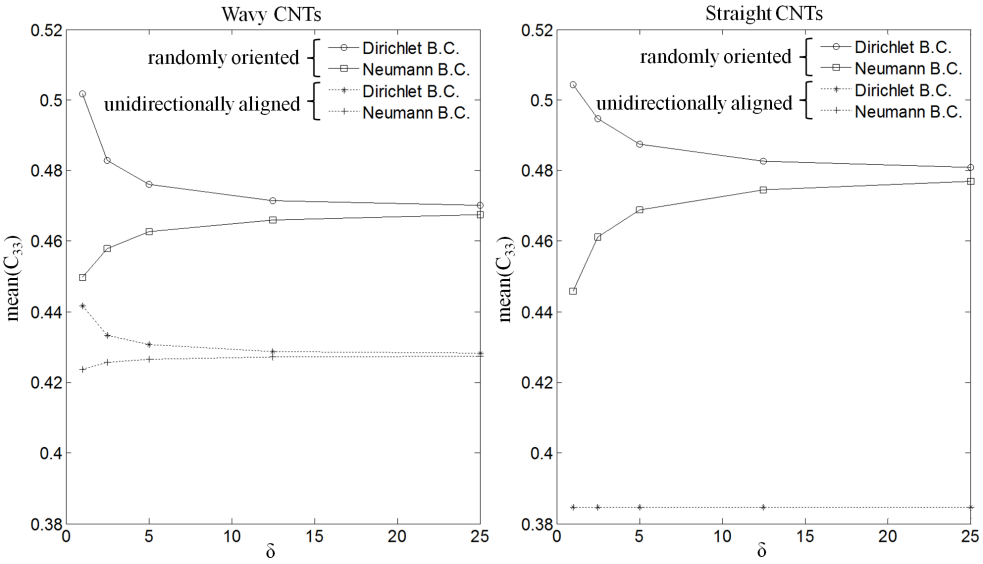

Figure 8: Comparison of numerical bounds of apparent property C_{33} for the composites of a) images 1, 2 and b) images 3, 4.

is considered, a mesoscale window of size $\delta \geq 5$ is required for composites containing randomly oriented CNTs, whereas a size $\delta > 12$ is required for composites containing unidirectionally aligned CNTs. If C_{33} is considered, $\delta \geq 5$ is an adequate size in order to attain the RVE with maximum 5% discrepancy for all the examined types of composites. A general observation is that CNT waviness has a relatively small effect on the RVE convergence rate, whereas the effect of orientation is dominant.

Fig. 10 illustrates the effect of waviness and orientation of CNTs on the level of anisotropy of the apparent elasticity tensor of the examined composites. Two measures are used to quantify anisotropy. The quantity $e^{C_{22}}_{C_{11}} = mean(|C_{11}-C_{22}|/2C_{22})$ and the isotropy indicator $\alpha_{iso} = mean(2C_{33}/(0.5(C_{11}-C_{22})-C_{12}))$. Note that the isotropy is approached as $e^{C_{22}}_{C_{11}}$ tends to zero and α_{iso} tends to unity. As expected, the unidirectionally aligned CNTs result in high level of anisotropy which is verified by both indicators. The level of anisotropy decreases with the increase of mesoscale size δ. This observation is in accordance with the assumption that at the RVE level the material can be considered isotropic in the mean sense.

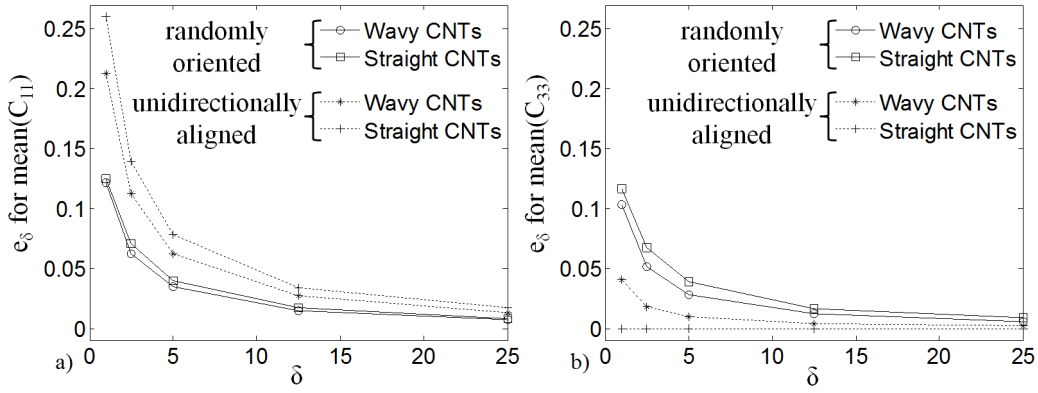

Figure 9: Discrepancy between upper and lower bounds of a) axial and b) shear stiffness with respect to mesoscale size δ for the composites of images 1-4.

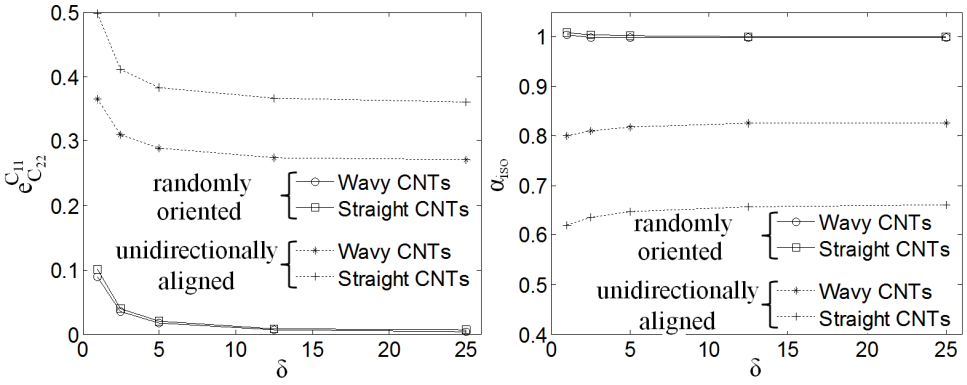

Figure 10: Effect of CNT waviness and orientation on the degree of anisotropy of the apparent elasticity tensor.

5.2. Determination of mesoscale random fields

In the context of stochastic multiscale analysis of composites with the stochastic finite element method, the material properties provided by the up-scaling procedure appear either as random fields (apparent properties in case of SVEs) or as random variables (effective properties in case of RVEs) [49, 50, 51]. As shown in section 5.1 the RVE for CNT-RCs cannot always be attained within an acceptable tolerance.

In this section, random fields for the axial stiffness component C_{11} of the apparent elasticity tensor of CNT-RCs are extracted for various mesoscale sizes δ. For this purpose a large number of SVE models are generated using the moving window technique as explained in section 3 and analyzed as described in section 4.1. Specifically, the random fields are calculated at δ =2.5, 5 and 12.5 by simulating n_w =5929, 1369 and 169 SVE models under kinematic uniform boundary conditions.

Figs. 11-14 depict the computed random fields along with the respective empirical distributions and 2-D spatial correlations of C_{11} at the aforementioned three mesoscale sizes δ for the composites of images 1-4, respectively. Note that the spatial correlations ρ_A^B have been calculated for every lag $(\xi_x,\ \xi_y)$ according to the following formula:

$$\rho_A^B\left(\xi_x,\ \xi_y\right) = \frac{1}{n_w - 1}\sum_{i=0}^{\sqrt{n_w}}\sum_{j=0}^{\sqrt{n_w}}\left(\frac{A\left(x_i,\ y_j\right) - \bar{A}}{\sigma_A}\right)\left(\frac{B\left(x_i + \xi_x,\ y_j + \xi_y\right) - \bar{B}}{\sigma_B}\right)$$

$$-\sqrt{n_w}\Delta\xi \leq \xi_x \leq \sqrt{n_w}\Delta\xi\ ,\ -\sqrt{n_w}\Delta\xi \leq \xi_y \leq \sqrt{n_w}\Delta\xi \tag{32}$$

with ρ_A^B denoting auto-correlations when quantity $A \equiv B$, otherwise cross-correlations are defined. $\bar{A}$, $\bar{B}$ are the spatial average values while σ_A, σ_B are the standard deviations of quantities A, B, respectively. A general observation for all mesoscale random fields is that their empirical PDFs become narrower as the mesoscale size δ increases. In other words, the random field tends to a random variable and thus the SVE tends to the RVE as δ increases. As it can be observed from all the examined composites, the variability of the apparent stiffness property is larger for smaller sizes δ. However, the randomly oriented CNTs result in small variability of the apparent property of the composites even at small sizes δ, compared to the unidirectionally aligned CNTs. The auto-correlations for lag $(\xi_x = 0,\ \xi_y = 0)$ are 1 and tend to zero for lag values $|\xi_x| > L$ and $|\xi_y| > L$.

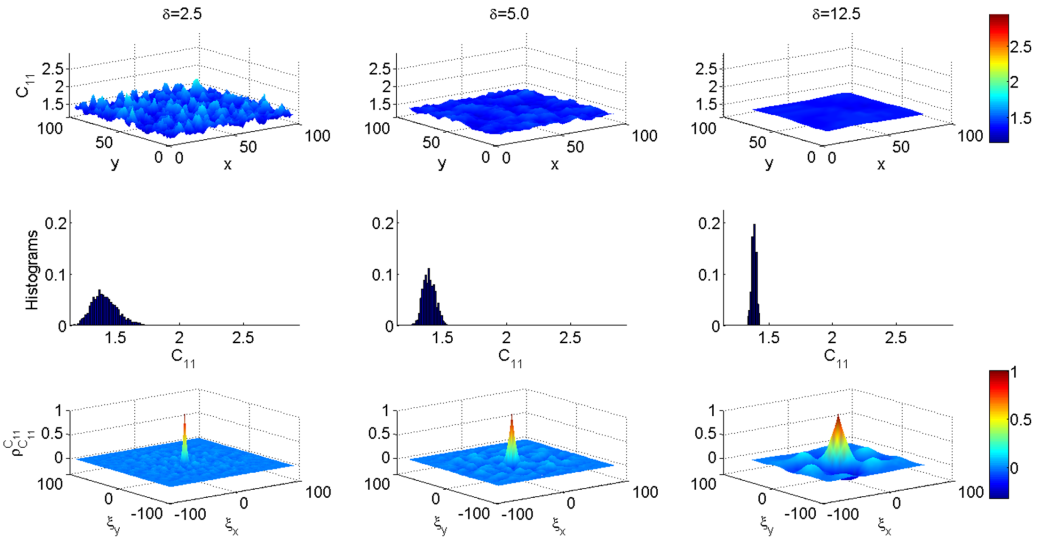

Figure 11: Mesoscale random fields for the axial stiffness C_{11} for the composite of image 1.

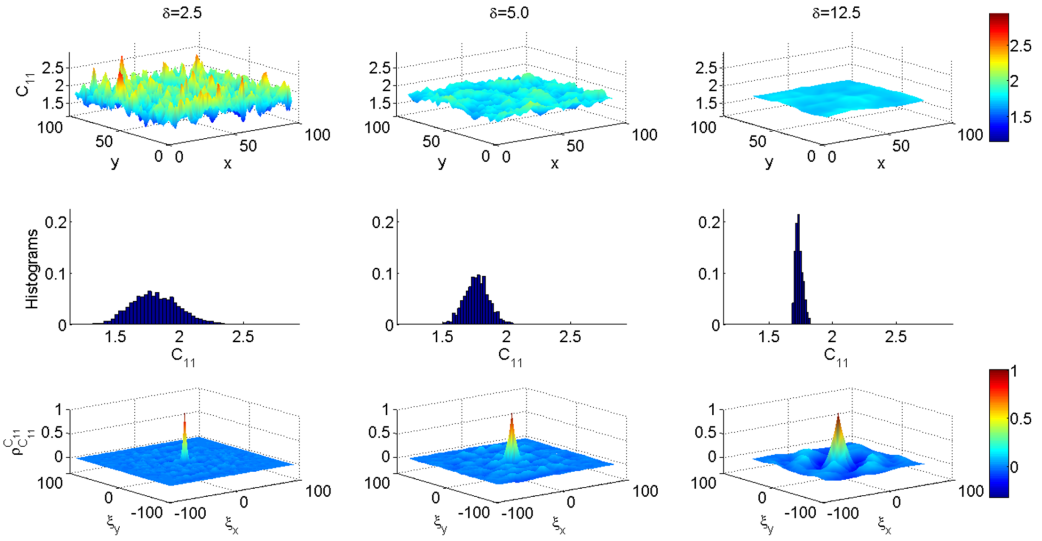

Figure 12: Mesoscale random fields for the axial stiffness C_{11} for the composite of image 2.

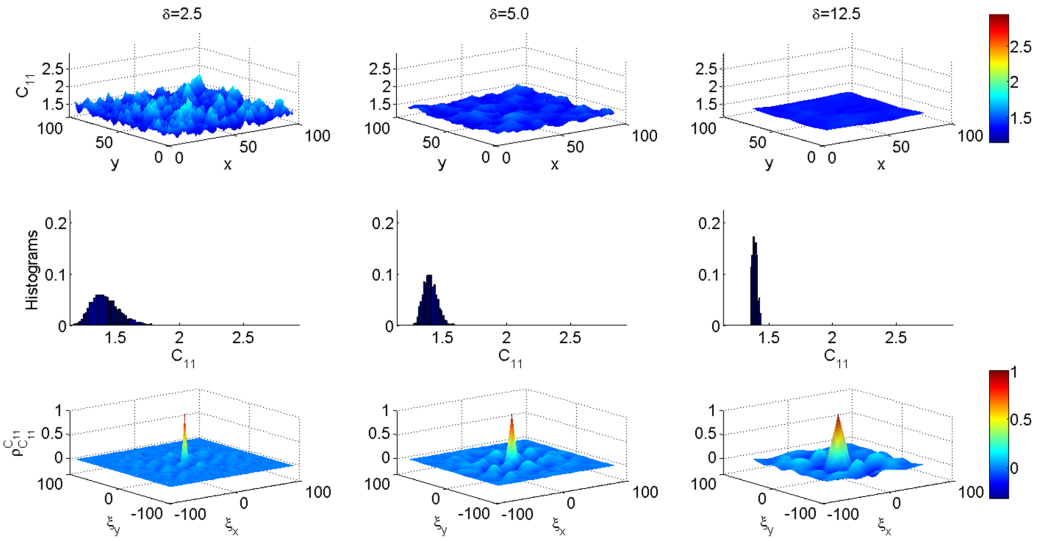

Figure 13: Mesoscale random fields for the axial stiffness C_{11} for the composite of image 3.

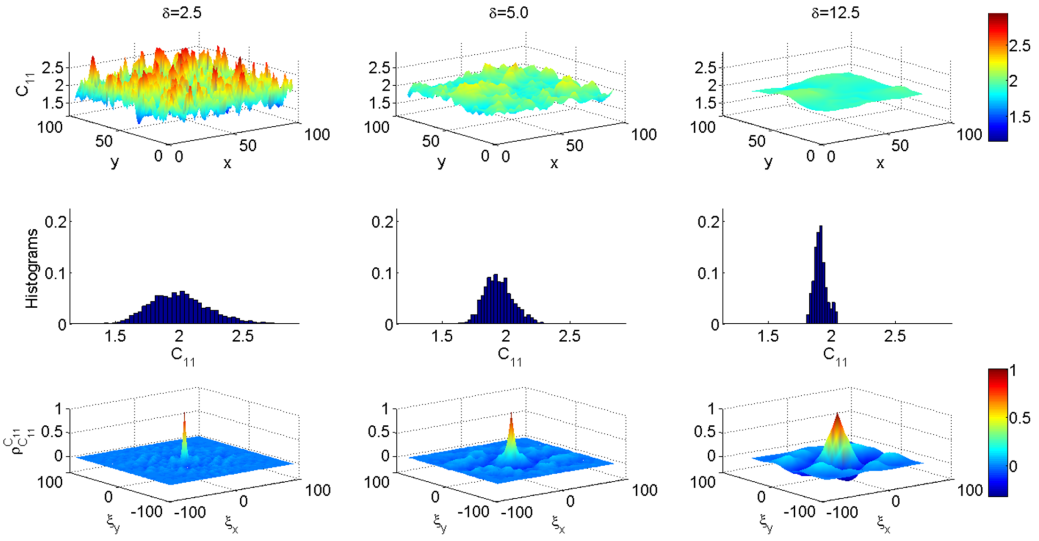

Figure 14: Mesoscale random fields for the axial stiffness C_{11} for the composite of image 4.

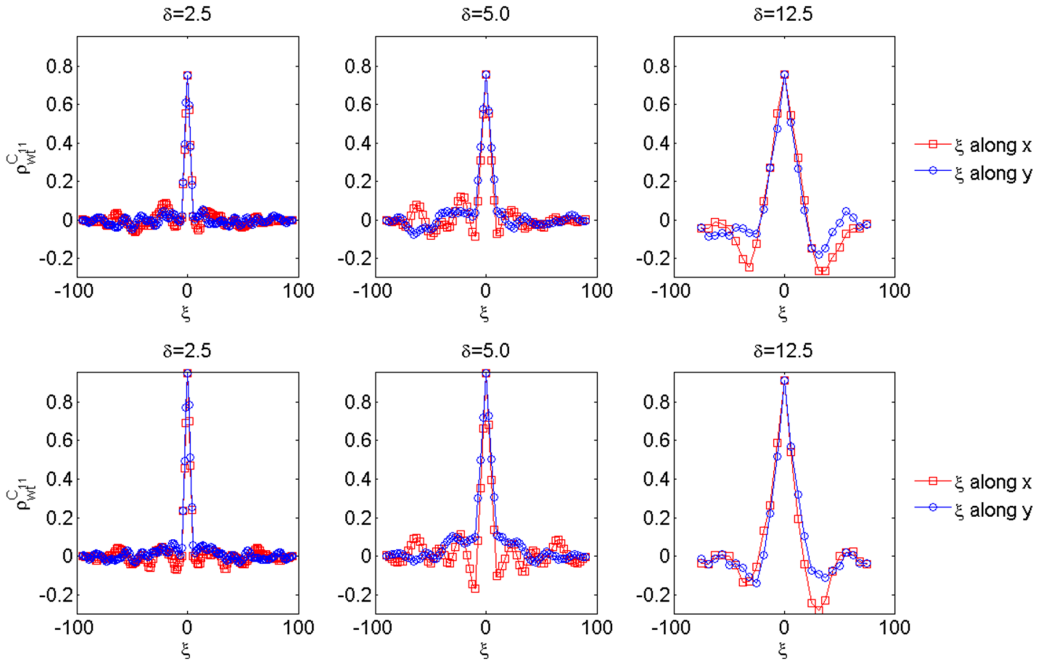

Figure 15: Cross correlations $\rho_{wt}^{C_{11}}$ at $(\xi_x,\ \xi_y = 0)$ and $(\xi_x = 0,\ \xi_y)$ for the composites of images 1-2.

The 1-D cross correlations $\rho_{wt}^{C_{11}}$ and $\rho_{C_{22}}^{C_{11}}$ are depicted in Figs. 15-16 and Figs. 17-18, respectively, for lag values along x $(\xi_x,\ \xi_y = 0)$ and y $(\xi_x = 0,\ \xi_y)$. The first row of these figures corresponds to composites with randomly oriented CNTs while the second row to composites with unidirectionally aligned CNTs. All cross-correlations are between -1 and +1 and tend to zero for $|\xi_x| > L$ or $|\xi_y| > L$. This can be attributed to the fact that the probability of SVE models to share common CNT reinforcements decreases as the length of the vector $\vec{\xi}_p$ (see Fig. 5) increases. As expected, the cross-correlation between C_{11} and C_{22} becomes negligible for the composite reinforced with straight unidirectionally aligned CNTs (see second row of Fig. 18).

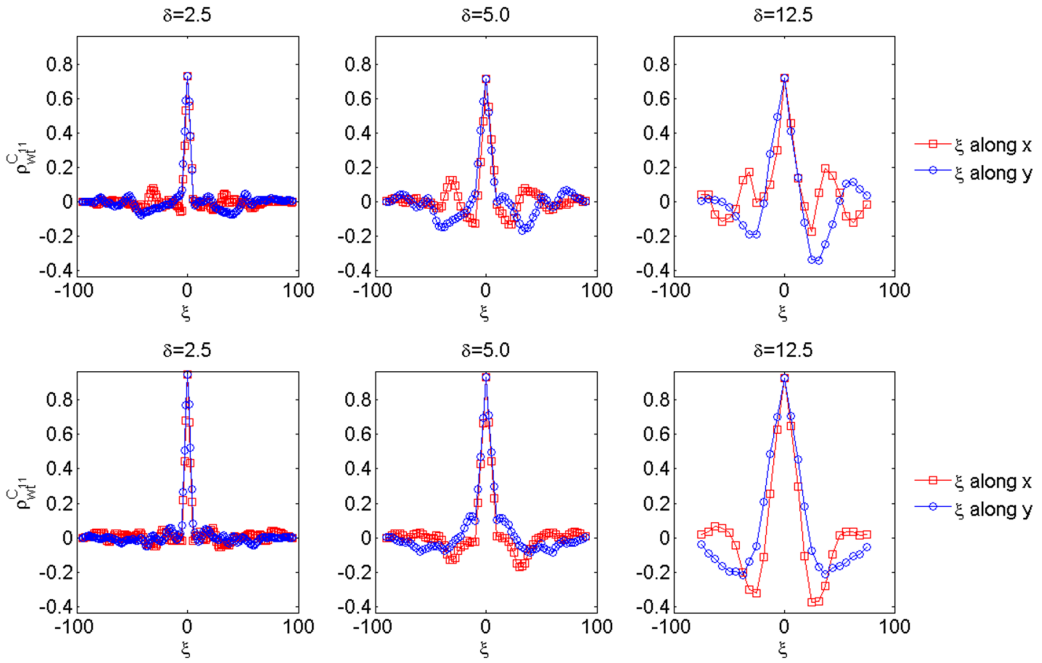

Figure 16: Cross correlations $\rho_{wt}^{C_{11}}$ at $(\xi_x,\ \xi_y = 0)$ and $(\xi_x = 0,\ \xi_y)$ for the composites of images 3-4.

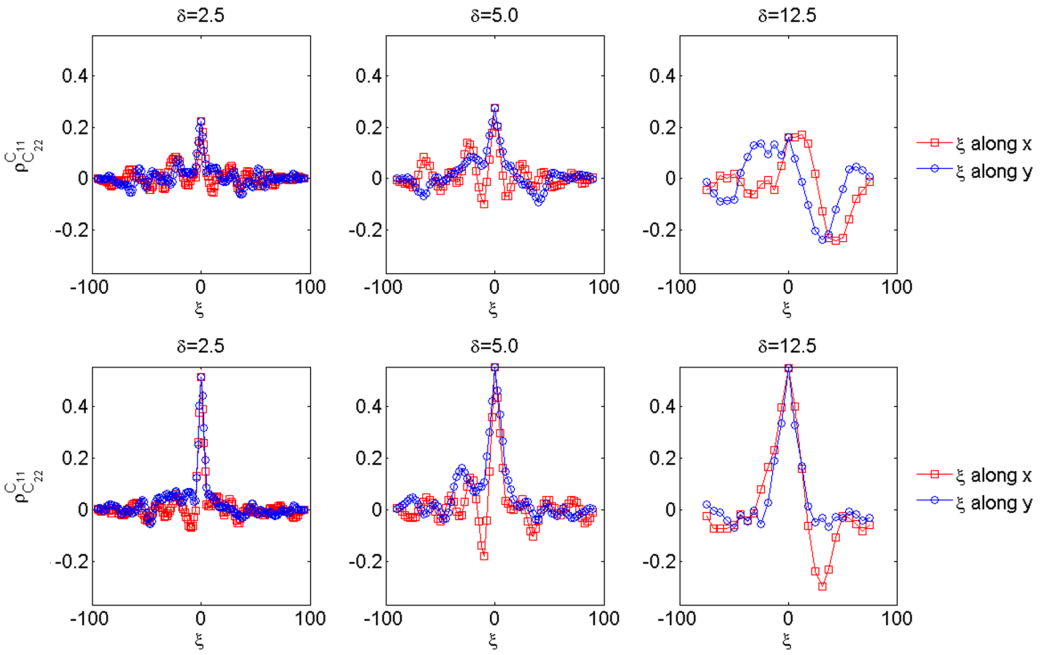

Figure 17: Cross correlations $\rho_{C_{22}}^{C_{11}}$ at $(\xi_x,\ \xi_y = 0)$ and $(\xi_x = 0,\ \xi_y)$ for the composites of images 1-2.

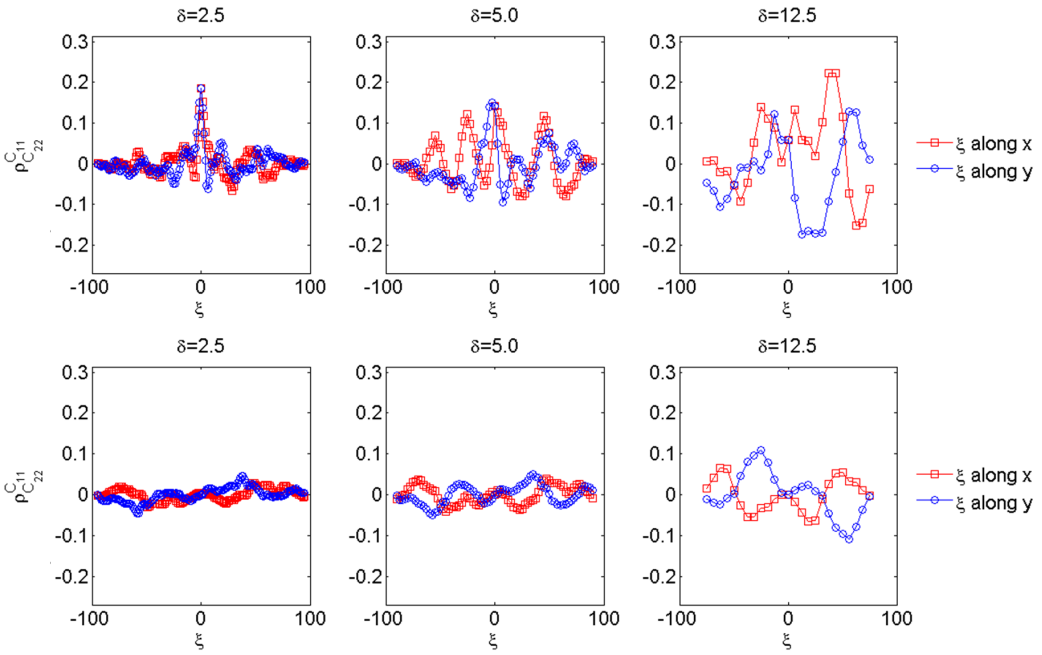

Figure 18: Cross correlations $\rho_{C_{22}}^{C_{11}}$ at $(\xi_x,\ \xi_y = 0)$ and $(\xi_x = 0,\ \xi_y)$ for the composites of images 3-4.

6. Conclusions

In this paper, a novel computational procedure has been proposed for the extraction of mesoscale random fields as well as for the determination of RVE size of CNT reinforced composites. The method can be applied to composites containing randomly dispersed CNTs with random waviness and orientation. The effect of the above uncertain morphological parameters on the apparent material properties and RVE size of CNT-RCs has been assessed. Specifically, by processing different computer-simulated images of random CNT reinforced composites, a variable number of statistical volume elements has been generated using the moving window technique. The local weight fraction variability, present in this kind of composites due to the random scattering of CNTs, has been calculated from the set of the aforementioned SVE models. A multiscale equivalent continuum modeling approach has been adopted to simulate CNTs, while real measurements have been used for the stochastic description of the random CNT waviness. Finite element models of the CNT-RC SVEs with simple meshes have been constructed by exploiting the embedded element technique. The discretized models were subjected to both kinematic and static uniform boundary conditions and by combining computational homogenization with Monte Carlo simulation the response statistics of the apparent material properties were calculated. The presented numerical results demonstrate that the effect of CNT waviness on the determination of RVE size is minimal, while CNT orientation has the dominant effect. The RVE must be attained with regard to a specific monitored component of the apparent elasticity tensor. Finally, it was shown that for sizes smaller than the RVE, mesoscale random fields for the apparent material properties can be obtained from the proposed computational procedure, which could be used in the context of stochastic finite element analysis of composite structures.

Acknowledgements

The financial support provided by the European Research Council Advanced Grant "MASTER - Mastering the computational challenges in numerical modeling and optimum design of CNT reinforced composites" (ERC-2011-ADG 20110209) is gratefully acknowledged by the authors. The support provided by the Research Committee of the Aristotle University of Thessaloniki is also gratefully acknowledged.

References

[1] B. Demczyk, Y. Wang, J. Cumings, M. Hetman, W. Han, A. Zettl, R. Ritchie, Direct mechanical measurement of the tensile strength and elastic modulus of multiwalled carbon nanotubes, Materials Science and Engineering: A 334 (1) (2002) 173–178.

[2] M.-F. Yu, O. Lourie, M. J. Dyer, K. Moloni, T. F. Kelly, R. S. Ruoff, Strength and breaking mechanism of multiwalled carbon nanotubes under tensile load, Science 287 (5453) (2000) 637–640.

[3] J.-P. Salvetat, J.-M. Bonard, N. Thomson, A. Kulik, L. Forro, W. Benoit, L. Zuppiroli, Mechanical properties of carbon nanotubes, Applied Physics A 69 (3) (1999) 255–260.

[4] S. Iijima, et al., Helical microtubules of graphitic carbon, nature 354 (6348) (1991) 56–58.

[5] D. Savvas, V. Papadopoulos, M. Papadrakakis, The effect of interfacial shear strength on damping behavior of carbon nanotube reinforced composites, International Journal of Solids and Structures 49 (26) (2012) 3823–3837.

[6] E. T. Thostenson, C. Li, T.-W. Chou, Nanocomposites in context, Composites Science and Technology 65 (3) (2005) 491–516.

[7] M. Arroyo, T. Belytschko, Finite crystal elasticity of carbon nanotubes based on the exponential Cauchy-Born rule, Physical Review B 69 (11) (2004) 115415.

[8] T. Chang, H. Gao, Size-dependent elastic properties of a single-walled carbon nanotube via a molecular mechanics model, Journal of the Mechanics and Physics of Solids 51 (6) (2003) 1059–1074.

[9] Y. Jin, F. Yuan, Simulation of elastic properties of single-walled carbon nanotubes, Composites Science and Technology 63 (11) (2003) 1507–1515.

[10] B. P. Grady, Carbon nanotube-polymer composites: manufacture, properties, and applications, John Wiley & Sons, 2011.

[11] D. Qian, W. K. Liu, Q. Zheng, Concurrent quantum/continuum coupling analysis of nanostructures, Computer Methods in Applied Mechanics and Engineering 197 (41) (2008) 3291–3323.

[12] J. Wernik, S. A. Meguid, Coupling atomistics and continuum in solids: status, prospects, and challenges, International Journal of Mechanics and Materials in Design 5 (1) (2009) 79–110.

[13] G. Odegard, T. Gates, K. Wise, C. Park, E. Siochi, Constitutive modeling of nanotube–reinforced polymer composites, Composites science and technology 63 (11) (2003) 1671–1687.

[14] W. Lu, J. Wu, J. Song, K. Hwang, L. Jiang, Y. Huang, A cohesive law for interfaces between multi-wall carbon nanotubes and polymers due to the van der Waals interactions, Computer Methods in Applied Mechanics and Engineering 197 (41) (2008) 3261–3267.

[15] A. Needleman, T. Borders, L. Brinson, V. Flores, L. Schadler, Effect of an interphase region on debonding of a CNT reinforced polymer composite, Composites Science and Technology 70 (15) (2010) 2207–2215.

[16] H. Tan, L. Jiang, Y. Huang, B. Liu, K. Hwang, The effect of van der Waals-based interface cohesive law on carbon nanotube-reinforced composite materials, Composites Science and Technology 67 (14) (2007) 2941–2946.

[17] K. Tserpes, P. Papanikos, G. Labeas, S. G. Pantelakis, Multi-scale modeling of tensile behavior of carbon nanotube-reinforced composites, Theoretical and applied fracture mechanics 49 (1) (2008) 51–60.

[18] D. Savvas, V. Papadopoulos, Nonlinear multiscale homogenization of carbon nanotube reinforced composites with interfacial slippage, International Journal for Multiscale Computational Engineering 12 (4) (2014) 271–289.

[19] R. Bradshaw, F. Fisher, L. Brinson, Fiber waviness in nanotube-reinforced polymer composites-II: modeling via numerical approximation of the dilute strain concentration tensor, Composites Science and Technology 63 (11) (2003) 1705–1722.

[20] D.-L. Shi, X.-Q. Feng, Y. Y. Huang, K.-C. Hwang, H. Gao, The effect of nanotube waviness and agglomeration on the elastic property of carbon nanotube-reinforced composites, Journal of Engineering Materials and Technology 126 (3) (2004) 250–257.

[21] V. Anumandla, R. F. Gibson, A comprehensive closed form micromechanics model for estimating the elastic modulus of nanotube-reinforced composites, Composites Part A: Applied Science and Manufacturing 37 (12) (2006) 2178–2185.

[22] L. Shao, R. Luo, S. Bai, J. Wang, Prediction of effective moduli of carbon nanotube–reinforced composites with waviness and debonding, Composite Structures 87 (3) (2009) 274–281.

[23] E. Shady, Y. Gowayed, Effect of nanotube geometry on the elastic properties of nanocomposites, Composites Science and Technology 70 (10) (2010) 1476–1481.

[24] C. Miehe, A. Koch, Computational micro-to-macro transitions of discretized microstructures undergoing small strains, Archive of Applied Mechanics 72 (4-5) (2002) 300–317.

[25] S. Torquato, Random Heterogeneous Materials: Microstructure and Macroscopic Properties, Springer, New York, 2002.

[26] T. I. Zohdi, P. Wriggers, An Introduction to Computational Micromechanics, 2nd Edition, Lecture Notes in Applied and Computational Mechanics, vol. 20, Springer, Heidelberg, 2008.

[27] M. Geers, V. Kouznetsova, W. Brekelmans, Multi-scale computational homogenization: Trends and challenges, Journal of Computational and Applied Mathematics 234 (7) (2010) 2175–2182.

[28] R. Rafiee, Influence of carbon nanotube waviness on the stiffness reduction of CNT/polymer composites, Composite Structures 97 (2013) 304–309.

[29] Y. Su, Z. Li, L. Jiang, X. Gong, G. Fan, D. Zhang, Computational structural modeling and mechanical behavior of carbon nanotube reinforced aluminum matrix composites, Materials Science and Engineering: A 614 (2014) 273–283.

[30] S. Dong, J. Zhou, H. Liu, D. Qi, Computational prediction of waviness and orientation effects in carbon nanotube reinforced metal matrix composites, Computational Materials Science 101 (2015) 8–15.

[31] I. Y. Stein, B. L. Wardle, Mechanics of aligned carbon nanotube polymer matrix nanocomposites simulated via stochastic three-dimensional morphology, Nanotechnology 27 (3) (2015) 7.

[32] R. Hill, Elastic properties of reinforced solids: some theoretical principles, Journal of the Mechanics and Physics of Solids 11 (5) (1963) 357–372.

[33] T. Kanit, S. Forest, I. Galliet, V. Mounoury, D. Jeulin, Determination of the size of the representative volume element for random composites: statistical and numerical approach, International Journal of solids and structures 40 (13) (2003) 3647–3679.

[34] M. Silani, H. Talebi, S. Ziaei-Rad, P. Kerfriden, S. P. Bordas, T. Rabczuk, Stochastic modelling of clay/epoxy nanocomposites, Composite Structures 118 (2014) 241–249.

[35] J. Wimmer, B. Stier, J.-W. Simon, S. Reese, Computational homogenisation from a 3D finite element model of asphalt concrete–linear elastic computations, Finite Elements in Analysis and Design 110 (2016) 43–57.

[36] M. Ostoja-Starzewski, X. Wang, Stochastic finite elements as a bridge between random material microstructure and global response, Computer Methods in Applied Mechanics and Engineering 168 (1) (1999) 35–49.

[37] D. Savvas, G. Stefanou, M. Papadrakakis, Determination of RVE size for random composites with local volume fraction variation, Computer Methods in Applied Mechanics and Engineering (in press, 2016).

[38] W. Song, V. Krishnaswamy, R. V. Pucha, Computational homogenization in RVE models with material periodic conditions for CNT polymer composites, Composite Structures 137 (2016) 9–17.

[39] C. Li, T.-W. Chou, A structural mechanics approach for the analysis of carbon nanotubes, International Journal of Solids and Structures 40 (10) (2003) 2487–2499.

[40] D. Schillinger, V. Papadopoulos, Accurate estimation of evolutionary power spectra for strongly narrow-band random fields, Computer Methods in Applied Mechanics and Engineering 199 (17) (2010) 947–960.

[41] L. Cohen, Time-frequency analysis, vol. 778, Prentice Hall PTR Englewood Cliffs, New Jersey, 1995.

[42] D. E. Newland, Wavelet analysis of vibration. I: Theory, Journal of vibration and acoustics 116 (4) (1994) 409–416.

[43] P. D. Spanos, J. Tezcan, P. Tratskas, Stochastic processes evolutionary spectrum estimation via harmonic wavelets, Computer Methods in Applied Mechanics and Engineering 194 (12) (2005) 1367–1383.

[44] M. Broggi, G. Schuëller, Efficient modeling of imperfections for buckling analysis of composite cylindrical shells, Engineering Structures 33 (5) (2011) 1796–1806.

[45] M. Shinozuka, C.-M. Jan, Digital simulation of random processes and its applications, Journal of sound and vibration 25 (1) (1972) 111–128.

[46] Z. Shan, A. M. Gokhale, Representative volume element for non-uniform micro-structure, Computational Materials Science 24 (3) (2002) 361–379.

[47] S. H. R. Sanei, R. S. Fertig, Uncorrelated volume element for stochastic modeling of microstructures based on local fiber volume fraction variation, Composites Science and Technology 117 (2015) 191–198.

[48] P. M. Suquet, Elements of homogenization for inelastic solid mechanics, in: E. Sanchez-Palencia and A. Zaoui, Eds., Homogenization Techniques for Composite Media, Springer, 193–278, 1987.

[49] G. Stefanou, The stochastic finite element method: past, present and future, Computer Methods in Applied Mechanics and Engineering 198 (9) (2009b) 1031–1051.

[50] A. Kucerová, H. Matthies, Uncertainty updating in the description of heterogeneous materials, Technische Mechanik 30 (1-3) (2010) 211–226.

[51] G. Stefanou, D. Savvas, M. Papadrakakis, Stochastic finite element analysis of composite structures based on material microstructure, Composite Structures 132 (2015) 384–392.